Pure Appl. Geophys. 175 (2018), 2975–2986
© 2018 Springer International Publishing AG, part of Springer Nature
https://doi.org/10.1007/s00024-018-1806-0

Pure and Applied Geophysics

Modeling Poroelastic Wave Propagation in a Real 2-D Complex Geological Structure Obtained via Self-Organizing Maps

Reymundo Itzá Balam,[1] Ursula Iturrarán-Viveros,[1] and Jorge O. Parra[2]

Abstract—Two main stages of seismic modeling are geological model building and numerical computation of seismic response for the model. The quality of the computed seismic response is partly related to the type of model that is built. Therefore, the model building approaches become as important as seismic forward numerical methods. For this purpose, three petrophysical facies (sands, shales and limestones) are extracted from reflection seismic data and some seismic attributes via the clustering method called Self-Organizing Maps (SOM), which, in this context, serves as a geological model building tool. This model with all its properties is the input to the Optimal Implicit Staggered Finite Difference (OISFD) algorithm to create synthetic seismograms for poroelastic, poroacoustic and elastic media. The results show a good agreement between observed and 2-D synthetic seismograms. This demonstrates that the SOM classification method enables us to extract facies from seismic data and allows us to integrate the lithology at the borehole scale with the 2-D seismic data.

Key words: Implicit finite differences, poroelastic modeling, self-organizing maps, facies classification, seismic attributes.

1. Introduction

The characterization of wave propagation in complex geological structures is of fundamental importance in geophysics. In this paper, we focus on an exploration geophysics example: the data to be considered is a 3-D seismic survey acquired in an oil reservoir called the Waggoner Ranch located in northeast Texas. Production of this field is primarily from shallower Permian horizons, where thin sandstone and limestone formations represent alternating, fairly rapid transgressive and regressive marine sequences. The reservoir is a sand–shale sequence that is characterized at the borehole and seismic scales. The well-log data and the lithofacies are described in detail by Parra et al. (2006) and selected seismic reflection lines calibrated with well-logs are given in Parra et al. (2015). Three facies are extracted from this reflection seismic data by applying Self-Organizing Maps to a set of instantaneous seismic attributes derived from a 2-D section of the seismic data. The SOM serves as a geological model building tool that delineates the layers of sands, shales and limestones.

The Self-Organizing Maps (SOM) neural network algorithm is based on competitive and unsupervised learning. It was first proposed by Kohonen (1981, 1982) as a visualization tool and later revisited in the following references Kohonen (2001, 2013). It is mainly used for visualization and clustering of data and it constitutes one powerful data mining technique. Some of the geophysical applications are given in Roy et al. (2013) and Roy and Marfut (2012), where authors successfully apply SOM to identify diagenetically altered facies of the Mississippi Lime play. In Konaté et al. (2015) authors applied an SOM neural network in the classification of metamorphic rocks from Chinese Continental Scientific Drilling Main Hole log data. In Stankiewicz et al. (2010) the SOM has been used to identify classes that correspond to real geological formations. We refer to Bauer et al. (2008) and Klose (2006) for a tomography interpretation. Tselentis et al. (2011) implemented SOM to facilitate the lithological classification of the passive seismic tomography results. In Bauer et al. (2012) authors perform a classification of the litho-type distribution (in the northeast German

[1] Facultad de Ciencias, Universidad Nacional Autónoma de México, Circuito Escolar S/N, Coyoacán C.P. 04510, México D.F., México. E-mail: reymundo.itza@gmail.com; ursula@ciencias.unam.mx

[2] Southwest Research Institute, San Antonio, Texas, USA. E-mail: joparram@yahoo.com

Basin) combining seismic tomography and inversion of magnetotelluric data and use SOM to obtain interesting features such as the characteristic properties of the Jurassic interpreted as the signature of shales. In Saraswat and Sen (2012), the authors propose an artificial immune-based SOM. For waveform classification based on SOM, see Du et al. (2015) and Essenreiter et al. (2001).

Since the classic theory of wave propagation in poroelastic media was proposed by Maurice Biot (1956a, b), the problem of modeling wave propagation in poroelastic media has been widely studied using a variety of different numerical approaches. To mention but a few authors, see Carcione and Helle (1999) and Carcione and Quiroga-Goode (1995), they use a velocity–stress staggered grid performing time updates in an approximate two-step integration process. Zhu and McMechan (1991) investigate the effects of seismic displacements of the solid frame and of the fluids due to spatial variations in porosity, permeability and fluid viscosity using a second-order 2-D explicit scheme. Özdenvar and McMechan (1997) developed a pseudo-spectral method for solving poroelastic differential equations in a displacement formulation. Masson et al. (2006) developed a standard explicit time integration technique for solving Biot's equations. Carcione et al. (2010) provide a thorough review of the previous literature of computational poroelasticity.

Recently Liu and Sen (2009) developed efficient implicit space derivative operators using a staggered-grid scheme with even-order accuracy for first-order derivatives. The results showed that the finite difference (FD) accuracy tends to increase as the operator length increases and the wave number range drops. Liu (2014), shows an improvement of his method and proposed a LS-based scheme to derive globally Optimal FD coefficients for spatial derivatives, computing them over a given wave number range using the LS method. We apply the approach given in Itzá et al. (2016) where the authors used the OISFD method given in Liu (2014) to solve poroelastic equations (showing stability and dispersion analysis) to model the seismic data acquired at Waggoner Ranch.

There are various mathematical formulations to simulate wave propagation in a variety of media with different physical properties. However, all these tools are to some degree, simplifications of the real world. Consequently, they might not be good enough to measure the effects and the relative importance of the physical parameters. In our work, we illustrate the differences among elastic, poroacoustic and poroelastic models by computing synthetic seismograms in a complex model.

Using the well-log information and a rock physical analysis given in Parra et al. (2015) we can establish the physical properties of these three lithological units in this specific study area. Once we have determined the complex geological settings and its physical properties, this information will constitute the inputs to our numerical modeling technique.

In summary, in this paper we will proceed as follows: we first describe the SOM method that includes its theoretical basis and how it is used to construct a geological model for an oil and gas reservoir in northeast Texas. Secondly, we explain the modeling technique that is applied to simulate surface reflection seismic waves. Finally, we conduct numerical modeling, by comparing acquired real data and synthetic seismograms, to demonstrate the combined application of SOM and reservoir modeling.

2. SOM Method

2.1. Theory and Definition of Self-Organizing Maps

The Self-Organizing Maps consist of a set of N nodes or neurons $\{\eta_1, \eta_2, \ldots, \eta_N\}$ (the neurons outputs are real numbers) in a 2-D hexagonal, rectangular or irregular grid, also called retina. There are two dimensions for the retina which correspond to each direction and their product has to be the same as the total number of neurons, i.e. $N = \text{size } X \times \text{size } Y$. The number of neurons in the retina may range from a few dozen to several thousands. In most applications, it is chosen much smaller than the total number of data vectors. Hexagonal grids are more common since they allow more neurons to update their weights than rectangular grids because each neuron in the grid has direct contact with six neurons (immediate neighbors) instead of four; we use a hexagonal grid. An input vector $\mathbf{x} = (\xi_1, \xi_2, \ldots, \xi_n) \in \mathbb{R}^n$ (in this case, the inputs are the selected seismic attributes) is

connected in parallel to all neurons in the grid with some weights $\mathbf{w}_{ij}$ (also called reference vectors). In Fig. 1 an example of a SOM retina illustrates how the weights are connected to all the neurons in the retina and to all the inputs. For the relative size of the two axes (i.e. size X and size Y) of the retina, Kohonen (2013) suggested to use the ratio of the two largest eigenvalues from the covariance matrix analysis of the input data. Since these criteria indicate just a ratio between the sizes of the two axes, the precise size of the retina needs to be determined by a trial-and-error method; large maps take longer to train than smaller maps. According to our experiments, we have obtained the best results with a retina of size 11×11.

The main virtue of the SOM is the visualization of the data space, whereupon the clustering structures must be visible. There is no sense in using the SOM for very small data sets since there are better methods to analyze small data sets. The Self-Organizing Maps neural network is a quantizing method and has limited resolution to show the cluster structures, sometimes the data set may contain few clusters, so a coarse resolution is sufficient.

In this work we use the parallel Batch-Map learning mode which is a variant of the original sequential SOM (see Kohonen 2001 section 3.6, p.138). In the parallel Batch-Map version the weights update their values after presenting the full set of inputs.

Vesanto and Alhoniemi (2000) proposed a two-level approach for conducting clustering tasks, called SOM-Ward. Firstly, the data set is projected onto a two-dimensional retina using SOM (Batch-Map). Then the resulting SOM is divided into groups using the Ward's clustering algorithm. This is an agglomerative hierarchical clustering method that starts with a clustering in which each map node is treated as a separate cluster. The two clusters with minimum distance are merged in each step until there is only one cluster left in the map, see Ward (1963). SOM-Ward's clustering is a modification of Ward's algorithm which limits cluster agglomeration to topological neighboring nodes. After training the SOM we apply this hierarchical agglomerative clustering of the trained SOM, see Day and Edelsbrunner (1984). This is an advantage because for the case of large data sets, the clustering is done in a smaller number of samples (in the 2-D retina) than the original data set. In this case, the size of the retina is $11 \times 11 = 121$ instead of the total number of input vectors: number of traces $\times$ number of time samples $\times$ number of attributes $= 116 \times 501 \times 11 = 639,276$. This is a clear benefit in terms of computational time.

2.2. *Application of SOM to Construct the Geological Model*

We briefly describe how the seismic section with facies used in the numerical simulation was obtained. In order to train the SOM we used 11

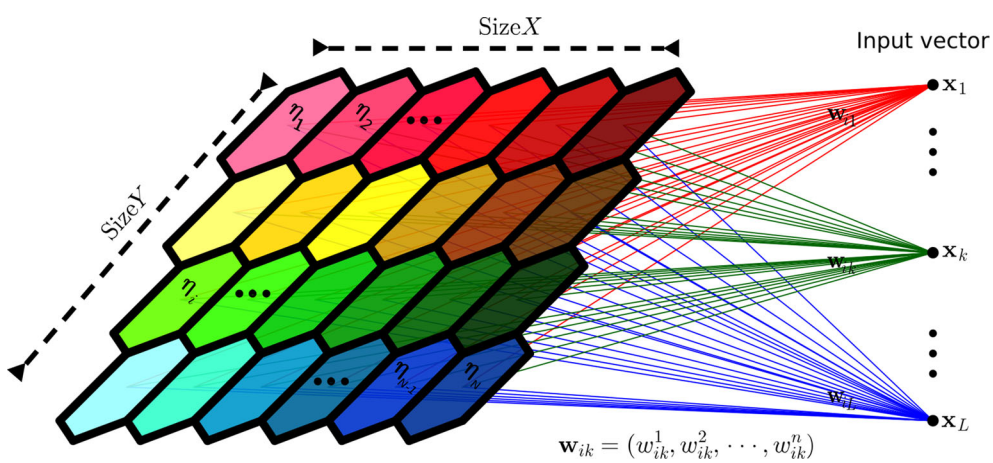

Figure 1
Example of a Self-Organizing Map retina with its neurons η_i, weights $\mathbf{w}_i$ and inputs $\mathbf{x}_i$

attributes as inputs: time; stacked seismic trace; Hilbert transform; envelope; phase; instantaneous frequency; thin bed indicator; instantaneous band width, decay; factor of attenuation Q; acceleration and semblance; which are defined in the following references: Barnes (2015), Chopra and Marfurt (2007) and Taner et al. (1979, 1994). The selection of these seismic attributes was done using SOM, starting with a wider selection of 23 attributes and discarding the redundant ones by keeping the ones that had different feature maps among them. The feature maps are the values of the weights related

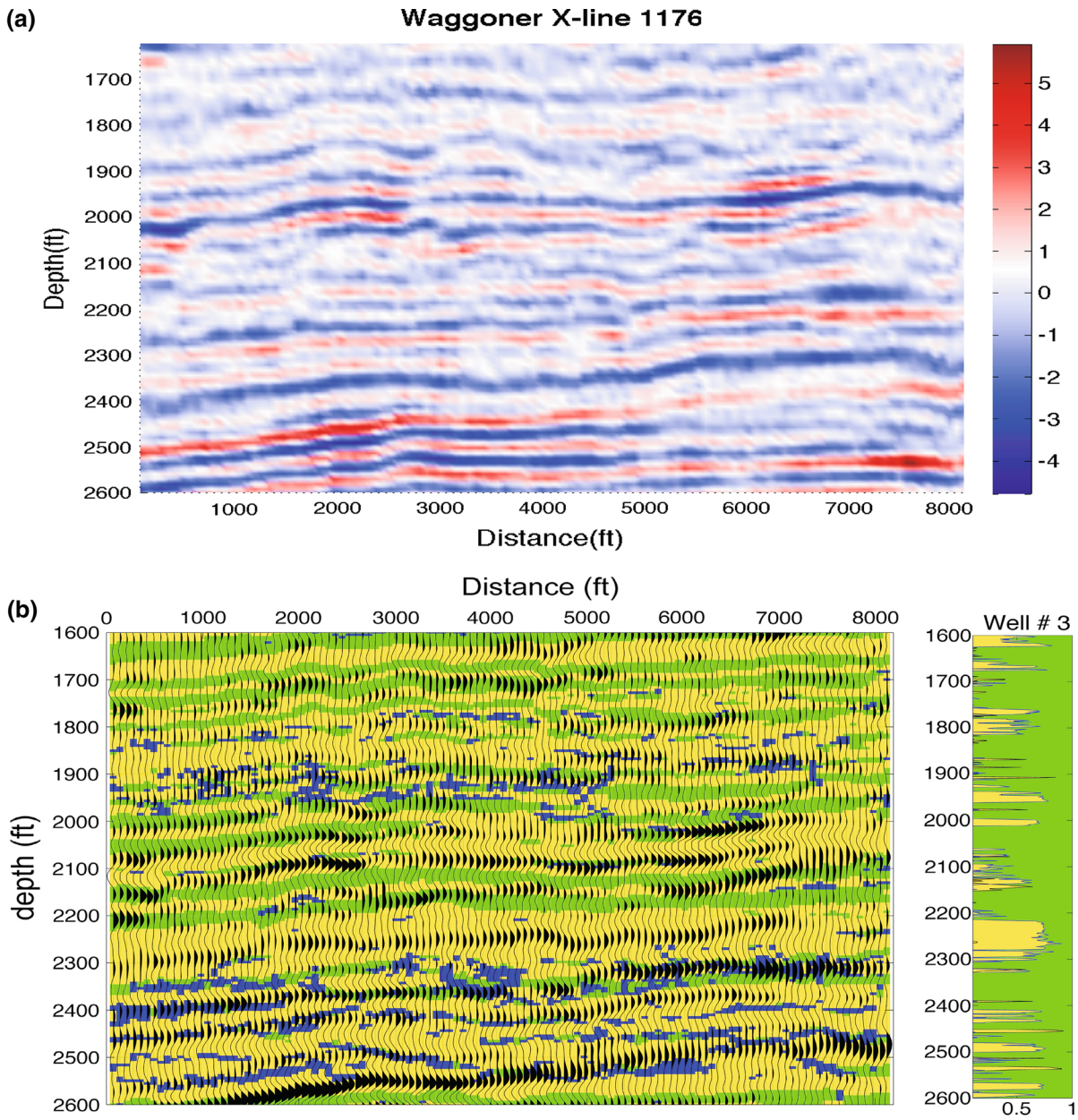

Figure 2
a The seismic section for the cross line 1176 of the Waggoner ranch. **b** Three seismic facies for the Waggoner seismic line: sands (yellow), shales (green) and limestones (blue) obtained using Self-Organizing Maps. In addition, we plot the facies that are computed directly from well-log data

to each attribute. This can be visualized in the retina with colors and it creates a color map of weights. If two ore more attributes have similar feature maps it implies that they have similar weight vectors. This fact suggest that these attributes are redundant and hence we keep those with different feature maps. This number of attributes determines the mathematical dimensionality of the input data. We used the free software called LabSOM[1] that allows us to use hierarchical agglomerative clustering of the trained SOM, see Day and Edelsbrunner (1984). The reservoir geology of the Waggoner Ranch is a sand and shale sequence with a small amount of limestone as markers. The Self-Organizing Maps use reflection attributes that are able to capture the three geological units. The SOM image correlates with the lithological units and the seismic reflection lines as well. The geological map obtained using SOM with three different facies (classes): sands (yellow), shales (green) and sandstones (blue) is shown in Fig. 2b. This map is a matrix of size 116 × 501 (= number of traces × number of time samples), which corresponds to the size of the seismic section. Each grid node has a label given by the clustering analysis (according to the interpretation analysis we selected three facies/labels). These three facies have certain physical properties given in Parra et al. (2015) and these constitute the input (the physical or real geological model) to the FD engine.

3. Modeling and Analysis

The first step of our analysis is to develop the algorithm to simulate synthetic waveforms in a heterogeneous reservoir. This requires finding the numerical solution of Biot's equations using a finite difference scheme, testing this solution with a simple model and then generating synthetic seismograms using the real geological model obtained with the SOM method.

[1] http://www.dynamics.unam.edu/DinamicaNoLineal3/labsom.htm.

3.1. Formulation

Following the work of Biot (1956a), we consider the velocity-stress formulation (low-frequency range) poroelastic equations. The system of equations is given by:

$$r^2\dot{v}_i = m\left(\tau_{xi,x} + \tau_{iz,z}\right) + \rho_f\left(bV_i + \delta_{xi}p_{,x} + \delta_{iz}p_{,z}\right) \tag{1}$$

$$r^2\dot{V}_i = -\rho_f\left(\tau_{xi,x} + \tau_{iz,z}\right) - \rho\left(bV_i + \delta_{xi}p_{,x} + \delta_{iz}p_{,z}\right) \tag{2}$$

$$\dot{\tau}_{ij} = \mu\left(v_{i,j} + v_{j,i}\right) + \delta_{ij}\left[\lambda_c\left(v_{x,x} + v_{z,z}\right) + \alpha M\left(V_{x,x} + V_{z,z}\right)\right] \tag{3}$$

$$\dot{p} = -\alpha M\left(v_{x,x} + v_{z,z}\right) - M\left(V_{x,x} + V_{z,z}\right) \tag{4}$$

where we denote by v_i = component of solid velocity, V_i = component of fluid velocity (relative to the the solid), δ_{ij} is the Kronecker delta, τ_{ij} are the stresses $(i,j \in \{x,z\})$, p is the pore pressure and $r^2 = m\rho - \rho_f^2$. The overall density of the saturated medium is determined by $\rho = \phi\rho_f + (1-\phi)\rho_s$, where ϕ is the porosity, ρ_f is the pore fluid density and ρ_s is the density of the solid grains. In an isotropic porous medium, we denote by K_s and K_f as the bulk moduli of the solid and fluid phases, K_{dry} and μ are the bulk and shear moduli of the porous material (dry or saturated). Then the poroelastic coefficient of effective stress is $\alpha = 1 - K_{\text{dry}}/K_s$ (this is also known as Biot & Willis constant, see Biot and Willis 1957), the coupling modulus between the solid and fluid is given by $M = \left[(\alpha-\phi)/K_s + \phi/K_f\right]^{-1}$ and the Lamé parameter of the saturated matrix is given by $\lambda_c = K_d - 2/3\mu + \alpha^2 M$. The effective fluid density is given by $m = T\rho_f/\phi$, where T is the tortuosity. Finally, $b = \eta/\kappa$ is called the friction coefficient (it is also called the mobility of the fluid), i.e. the ratio of fluid viscosity η and rock permeability κ (the usual hydrological permeability).

We perform the discretization as in Itzá et al. (2016), and then the space and time discretizations for the field variables are denoted by a sub-index or a super index respectively: $v_i^{n+1/2} = v_i(\mathbf{x}, t_{n+1/2})$, $V_i^{n+1/2} = V_i(\mathbf{x}, t_{n+1/2})$, $\tau_{ij}^n = \tau_{ij}(\mathbf{x}, t_n)$ and $p^n = p(\mathbf{x}, t_n)$ with $t_n = n\Delta t$. The approximations to spatial derivatives at the point $\mathbf{x}$ and direction x_k are given by $\partial f/\partial x_k|_{\mathbf{x}} \approx \Delta_k f$. Time discretization is done with a central differences scheme. The discretization yields:

$$v_i^{n+1/2} = v_i^{n-1/2} + A\Delta_j\tau_{ij}^n + B\Delta_i p^n + C\langle V_i^n\rangle \quad (5)$$

$$DV_i^{n+1/2} = V_i^{n-1/2} + EV_i^{n-1/2} + F\Delta_j\tau_{ij}^n + G\Delta_i p^n \quad (6)$$

$$\tau_{ij}^{n+1/2} = \tau_{ij}^{n-1/2} + H\left(\Delta_i v_j^n + \Delta_j v_i^n\right) + \left(I\Delta_i v_i^n + J\Delta_i V_i^n\right)\delta_{ij} \quad (7)$$

$$p^{n+1/2} = p^{n-1/2} - Jv_{i,i}^n + KV_{i,i}^n \quad (8)$$

where the notation $\langle\bullet\rangle$ means

$$\langle V_i^n\rangle = \left(V_i^{n+1/2} + V^{n-1/2}\right)/2 \quad (9)$$

The coefficients involved in (5–8) are given by:

$$\begin{aligned}
A &= (m\Delta t)/r^2\\
B &= (\rho_f\Delta t)/r^2\\
C &= (\rho_f b\Delta t)/(2r^2)\\
D &= 1 + \rho b\Delta t/(2r^2)\\
E &= -\rho b\Delta t/\left(2r^2\right)\\
F &= -\rho_f\Delta t/r^2\\
G &= \rho\Delta t/r^2\\
H &= \mu\Delta t\\
I &= \lambda_c\Delta t\\
J &= \alpha M\Delta t\\
K &= -M\Delta t
\end{aligned}$$

In order to compute the wave field over the entire staggered grid and since the material parameters are only defined on grid points with integer index, we need to compute averages of ρ_s, ρ_f, m and b on half-point grid nodes.

The horizontal component of velocity (v_x or V_x) uses the following harmonic averages:

$$\rho_{si,j+1/2} = \left[\frac{1}{2}\left(\frac{1}{\rho_{si,j}} + \frac{1}{\rho_{si,j+1}}\right)\right]^{-1} \quad \text{a similar formula for } \rho_f,$$

$$m_{i,j+1/2} = \left[\frac{1}{2}\left(\frac{1}{m_{i,j}} + \frac{1}{m_{i,j+1}}\right)\right]^{-1}$$

$$b_{i,j+1/2} = \left[\frac{1}{2}\left(\frac{1}{b_{i,j}} + \frac{1}{b_{i,j+1}}\right)\right]^{-1}.$$

While for the vertical component (v_z or V_z) we require:

$$\rho_{si+1/2,j} = \left[\frac{1}{2}\left(\frac{1}{\rho_{si,j}} + \frac{1}{\rho_{si+1,j}}\right)\right]^{-1} \quad \text{a similar formula for } \rho_f,$$

$$m_{i+1/2,j} = \left[\frac{1}{2}\left(\frac{1}{m_{i,j}} + \frac{1}{m_{i+1,j}}\right)\right]^{-1}$$

$$b_{i+1/2,j} = \left[\frac{1}{2}\left(\frac{1}{b_{i,j}} + \frac{1}{b_{i+1,j}}\right)\right]^{-1}.$$

To compute τ_{xz} we need the harmonic average of μ on grid points with a non-integer index:

$$\mu_{i+1/2,j+1/2} = \left[\frac{1}{4}\left(\frac{1}{\mu_{i,j}} + \frac{1}{\mu_{i,j+1}} + \frac{1}{\mu_{i+1,j}} + \frac{1}{\mu_{i+1,j+1}}\right)\right]^{-1}.$$

Finally, we do not need to use an average of parameters λ_c, α and M, because we only need them on grid points with an integer index.

3.2. Numerical Modeling

One approach widely used to compute synthetic seismograms in layered media is the use of propagator matrices (see for example, Aki and Richards 1980; Claerbout 1968; Haskell 1953, 1960, 1962; Kennett and Kerry 1979). The displacements at the top and bottom of the stack of layers are related by a product of propagator matrices, one for each layer. The response of the model includes the effects of all multiples. The advantage of this method is that, since it is an analytic solution, the computation is very fast and when one considers the full waveform inversion it could be an alternative to speed up the computation. On the contrary, this is a 1-D approach and does not capture the lateral variations of the physical properties (i.e. 2-D effects). Consequently, we choose the Optimal Implicit Finite Differences to solve numerically the set of Eqs. (1–4) with the physical properties that correspond to the facies illustrated in Fig. 2 obtained by the SOM method. The poroelastic parameters that correspond to this medium (these were obtained directly from well-log data) are given in Tables 1 and 2, see Parra et al. (2015). We have taken the velocity and the density for oil as $V_p = 1459$ m/s and $\rho_f = 827.7$ kg/m^3, see Higuti et al. (2001). In terms of saturating fluids, three depth intervals are considered: an upper and bottom interval

Table 1

Parameters for the Waggoner poroelastic model

	Depth intervals 1 and 3 (487.68–745.24 m) ∪ (749.81–792.48 m) saturated with brine			Depth interval 2 (745.24–749.81 m) saturated with oil			Units
	Limestone	Shale	Sand	Limestone	Shale	Sand	
V_p	5200	3309	3695	5427	3585	3700	m/s
V_s	2700	1653	2068	2789	1777	2040	m/s
K_f	2.25	2.25	2.25	1.8566	1.8566	1.8566	GPa
K_s	62	25	35	62	28	35	GPa
K_{dry}	45.746	17.422	15.461	43.452	21.261	16.482	GPa
ρ_s	2690	2540	2340	2700	2540	2380	kg/m^3
ρ_f	1000	1000	1000	872.2	872.2	872.2	kg/m^3
ϕ	0.18	0.17	0.2	0.012	0.15	0.16	–
η	1	1	1	1.729	1.729	1.729	cP
κ	1	0.01	200	1	0.01	200	mD
T	2	2	2	2	2	2	–

1cP = 10^{-3} Pa s; 1mD = 10^{-15} m^2

Table 2

Complementary parameters corresponding to the partial differential equation which describes the poroelastic model

	Depth intervals 1 and 3 (487.68–745.24 m) ∪ (749.81–792.48 m) saturated with brine			Depth interval 2 (745.24-749.81 m) saturated with oil			Units
	Limestone	Shale	Sand	Limestone	Shale	Sand	
m	11,110	11,760	10,000	145,400	11,630	10,900	Kg/m^3
ρ	2386	2278	2072	2678	2290	2139	Kg/m^3
b	1×10^{15}	1×10^{17}	5×10^{12}	1.729×10^{15}	1.729×10^{17}	8.645×10^{12}	Pa s/m^2
μ	19.61	6.940	10.01	21	8.021	9.905	GPa
α	0.026	0.303	0.382	0.299	0.241	0.529	
M	12.30	12.36	10.40	90.13	11.90	10.34	GPa
λ	33.52	13.93	10.30	37.52	16.60	12.77	GPa

saturated with brine, while the middle interval is saturated with oil.

The Self-Organizing Maps classification, yields a three-facies spatial classification (sands, shales and limestones); this allows us to provide lateral and vertical variations imposed by each facies. For any given position in space $(x, z) = (x, \text{depth})$ we have a facies assigned to it. Therefore, when setting up the physical parameters for that cell in the numerical modeling phase we assign the properties (in Tables 1 and 2) that correspond to the given depth interval.

The result of the SOM clustering, is a matrix of size 116×501 (= number of traces $\times$ number of time samples) which corresponds to the size of the seismic section. The physical distance between contiguous traces is 21.02 m. This matrix contains three different labels that represent the three facies: sand, shale and limestone. Therefore, the classification has a seismic scale and we have to reconcile this with the numerical mesh. From the 501 time samples (or facies labels) we need to consider only 156 time samples that lay in the study area which has a depth interval of [487.86, 792.57] m. The area that we need to model is larger in the x-direction than in the z-direction (i.e. depth). Therefore in order to have at least 6 nodes per wavelength we have to set a numerical mesh (i.e. a staggered grid) of size $Nx = 1624$, $Nz = 312$ with $\Delta x = 1.5$ m and $\Delta z = 0.976$ m. Since the reduced matrix of labels given by the SOM classification has size 116×156 we need a larger numerical mesh than

the given by the SOM labels. Consequently, in the x-direction we repeat 14 times each one of the 116 labels to obtain 1624 nodes (note that $116 \times 14 = 1624$). This is done dividing the area that is covered by the stations, i.e. 2438.4 m/1624 which gives $\Delta x = 1.5$ m. The physical properties of these numerical nodes are assigned according to the facies that was designated by the SOM to that trace. For the z-direction (depth) we perform a similar procedure. We need to model in depth a physical distance of 304.8 m and we have 156 time samples given by the seismic data and the SOM labels. We need $\Delta z = 0.976$ m, as a result, we repeat each row (corresponding to a time sample) to obtain 312 (= 156×2) grid nodes. With this setting we can ensure enough wavelength sampling for the range of frequencies considered and all the different velocities of the complex medium. For all numerical experiments the time step will be $\Delta t = 0.00001$ s. With this configuration we have on average 30 layers (per trace) with a minimum of 20 layers and a maximum of 39. These layers are set by the SOM clustering and they have different widths. For the first example, we use as the source function a Ricker wavelet:

$$S(t) = \exp\left(-2[tf_0 - 1.5]^2\right)\cos([tf_0 - 1.5]), \quad (10)$$

with central frequency $f_0 = 110$ Hz. The bulk source is located at the center of the numerical domain, i.e. in terms of grid points coordinates are $x_0 = 130$ and $z_0 = 812$. In Fig. 3 we illustrate the wave propagation in the Waggoner heterogeneous medium showing snapshots of displacements obtained from the OISFD scheme at time (a) $t = 0.05$ s, (b) $t = 0.14$ s, and (c) $t = 0.24$ s.

We simulate a more realistic source by transmitting a normal plane wave incident at the depth 487.68 m. In the resulting synthetic seismogram we remove the source effect because there is not a source applied at the depth of 487.68 m in the real data. The source used in this example is the wavelet extracted from the seismic data with central frequency $f_0 = 110$ Hz.

To demonstrate the use of the poroelastic modeling solution we select the data from Table 1 to compute seismic waveforms at the seismic scale so we can compare them with a select observed seismic trace at the well location. In Fig. 4 we compare the observed trace with synthetic seismograms for poroelastic, poroacoustic and elastic models (black, blue, purple and red wiggle traces, respectively). Firstly, in Fig. 5 we illustrate the full waveforms of the three models. The two vertical dashed black lines correspond to time window shown in Fig. 4, which corresponds to the main area of interest, since it includes the productive Milliham sand. As we expected the poroelastic and poroacoustic waveforms are more attenuated than the elastic waveform. The medium is partially saturated with hydrocarbons and brine; as a consequence the wave creates a deformation in the porous medium partially saturated with fluids. Viscous losses during the induced flow led to irreversible energy loss and the resulting wave attenuation (Parra et al. 2015). In addition, we noticed that the poroacoustic and poroelastic models produce traces with similar trends. These results are in agreement with Özdenvar and McMechan (1997); also in this paper, the authors suggest the use of the most complete model to get seismograms with correct scale. Whilst it is not expected that the OISFD and the SOM model reproduce the precise details of real data, synthetic data captures the main trends (reflections, including multiples, from the given layered model) of the real traces. From Fig. 4 we observe that the poroelastic model produces better approximations than the elastic and poroacoustic models. However, we adjust the trace scale before comparing with the real trace.

3.3. *Selection of the Frequency Range in the Numerical Model*

We calibrated the frequency to choose the one that produces the best results in terms of the comparison between real and synthetic data. According to Masson et al. (2006) the seismic band of frequency is loosely defined as $\omega/(2\pi) < 10$ kHz. The frequency we have chosen for the simulations is within the frequency spectra of the seismic trace that corresponds to the trace located at the well-bore. Most of the energy in Fig. 6 is within the range 5 – 130 Hz. Therefore we believe that the results are consistent with the data.

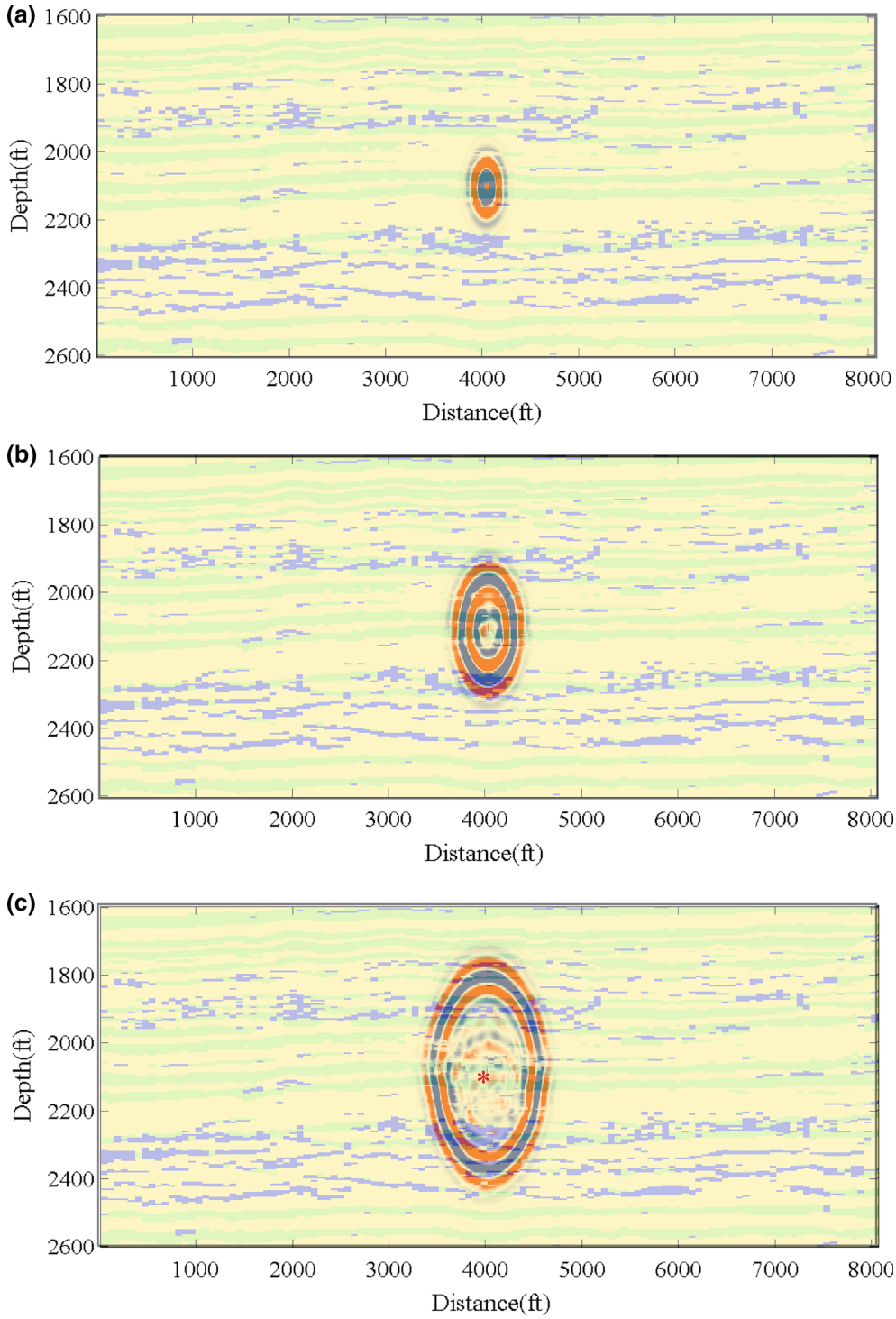

Figure 3
Snapshots of pressure obtained by the OISFD for the Waggoner heterogeneous poroelastic model at **a** $t = 0.05$ s, **b** $t = 0.14$ s, **c** $t = 0.24$ s

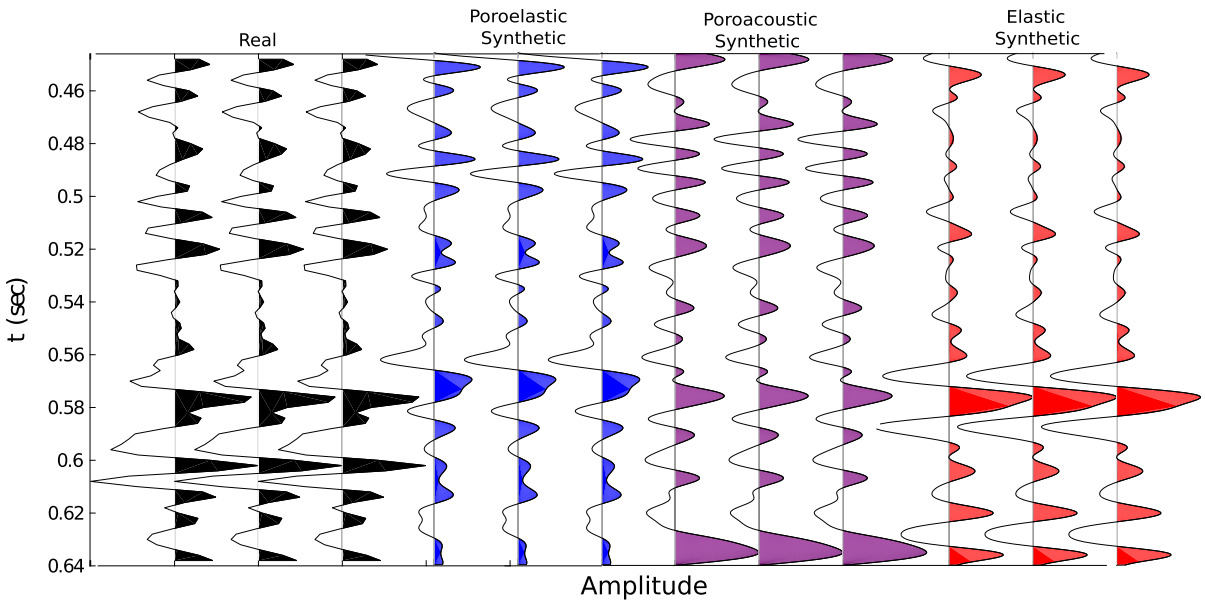

Figure 4
Comparison between the vertical component of the displacement in the solid, synthetic trace v_z, and real trace. The black wiggle traces correspond to the real data, whereas blue, purple and red correspond to poroelastic, poroacoustic and elastic modeling, respectively. We have chosen to show only the trace (repeated three times for each case) that corresponds to the well-log; however, similar trends are seen in the other traces of this seismic line. The time window shown in these seismograms corresponds to the interest zone where the Milliham productive sand is located

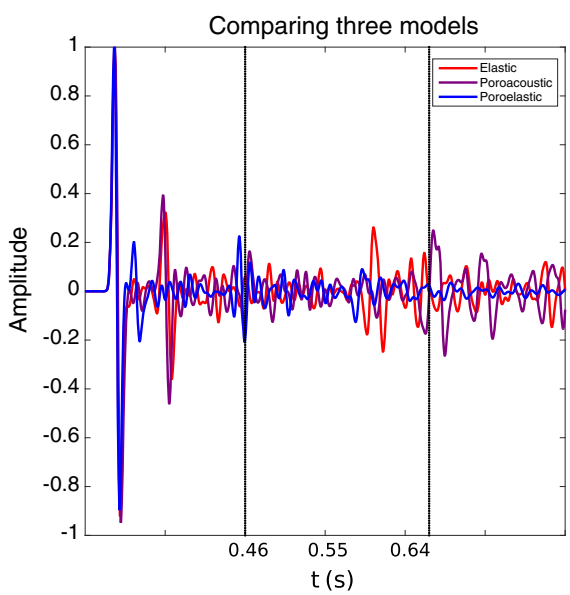

Figure 5
Vertical component of the displacement in the solid, synthetic trace v_z, of the elastic, poroacoustic and poroelastic models. The two vertical black lines correspond to the times shown in Fig. 4

4. Conclusions

The numerical results show that the geological setting obtained with the SOM constitutes an adequate description of the real data, since the synthetic traces resemble the acquired data. The elastic, poroacoustic and poroelastic models produce different results, as expected, and one of these differences is the amplitude. From these three models, the poroelastic model showed the best approximation although the poroacoustic model also captures the main trends of the real data. If a simple description of the medium response is required, then the poroacoustic model is enough. The poroelastic model could be use as a starting velocity model for a more complex full waveform inversion procedure. The Optimal FD provides an accurate forward modeling tool for complex geological structures. It should be noted that for the Optimal FD to be practical to calculate synthetic seismograms in an iterative procedure, such as full waveform inversion, more work is needed to implement the code in GPUs or other devices to

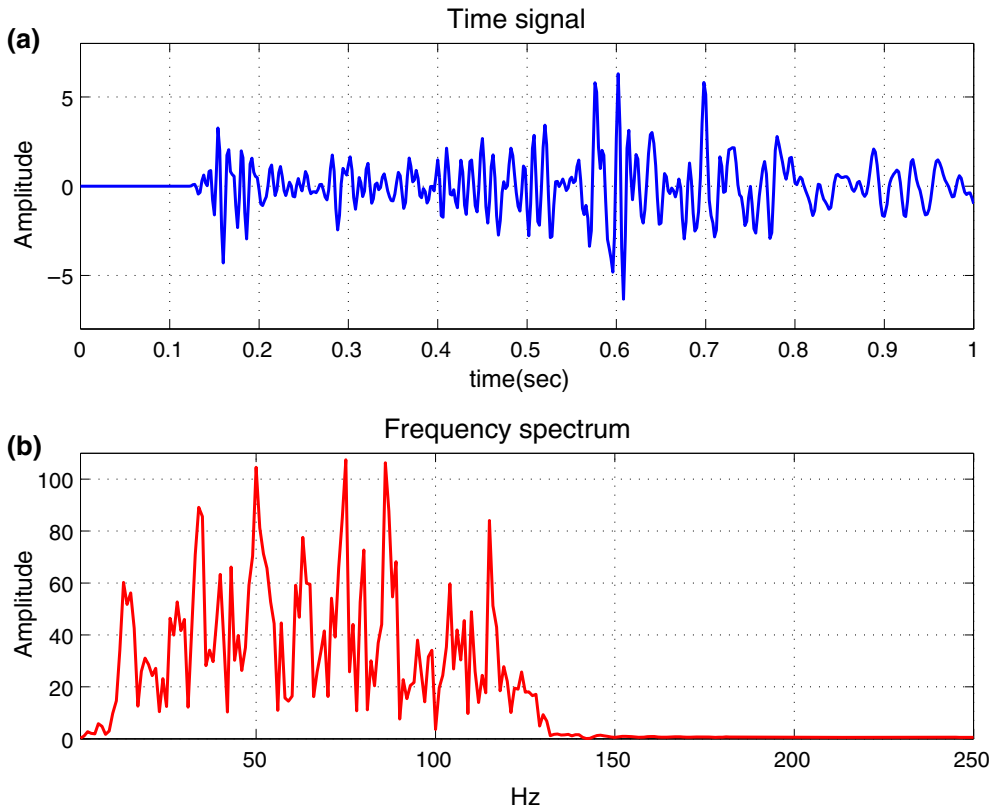

Figure 6
a Real seismic trace that corresponds to the well-bore and its **b** frequency spectrum of the seismic trace

speed up computations. Far-reaching implications on the physical parameters (permeability, porosity or fluid saturation) that are lowering the attenuation are important.

Other clustering techniques such as k-means, multivariate normal distributions, and density-based spatial clustering can be also applied and will be studied in future work.

Acknowledgements

We would like to thank the two anonymous reviewers and the editor Andrew R. Gorman for kind comments that helped to improve this manuscript. This work was partially supported by CONACYT Mexico under PROINNOVA projects 241763, 231476; DGAPA UNAM project number IN100917. We thank Todd Thomas and the W.T. Waggoner Estate for providing the data. Work by RIB was partially supported by a postdoctoral fellowship at CIMAT-Mérida provided by CONACYT grant FOMIX-YUC 221183.

References

Aki, K., & Richards, P. (1980). *Quantitative seismology: theory and methods*. San Francisco: W.H.Freeman and Co.

Barnes, A. E. (2015). *Hanbook of post-stack seismic attributes*. Tulsa: SEG.

Bauer, K., Munoz, G., & Moeck, I. (2012). Pattern recognition and lithological interpretation of collocated seismic and magnetotelluric models using self-organizing maps. *Geophysical Journal International*, *189*, 984–998.

Bauer, K., Part, R. G., Haberland, C., & Weber, M. (2008). Neural network analysis of crosshole tomographic images: the seismic signature of gas hydrate bearing sediments in the Mackenzie Delta (NW Canada). *Geophysical Research Letters*, *35*, 1–6.

Biot, M. A. (1956a). Theory of propagation of elastic waves in a fluid-saturated porous solid. I. Low frequency range. *The Journal of the Acoustical Society of America*, *28*, 168–178.

Biot, M. A. (1956b). Theory of propagation of elastic waves in a fluid-saturated porous solid. II. Higher frequency range. *The Journal of the Acoustical Society of America*, *28*, 179–191.

Biot, M. A., & Willis, D. G. (1957). The elastic coefficients of the theory of consolidation. *Journal of Applied Mechanics*, *24*, 594–601.

Carcione, J. M., & Helle, H. (1999). Numerical solution of poro-viscoelastic wave equation on a staggered grid. *Journal of Computational Physics*, *154*, 520–527.

Carcione, J. M., Morency, C., & Santos, J. E. (2010). Computatinal poroelasticity: a review. *Geophysics*, *75*(5), 75A229–75A243.

Carcione, J. M., & Quiroga-Goode, G. (1995). Some aspects of the physics and numerical modelling of Biot compressional waves. *Journal of Computational Acoustics*, *3*(4), 261–280.

Claerbout, J. (1968). Synthesis of a layered medium from its acoustic transmission response. *Geophysics*, *33*(2), 264–269.

Chopra, S., & Marfurt, K. (2007). *Seismic attributes for prospect identification and reservoir characterization. Geophysical development series*. Tulsa: Society of Exploration Geophysicists.

Day, W. H., & Edelsbrunner, H. (1984). Efficient algorithms for agglomerative hierarchical clustering methods. *Journal of Cclassification*, *1*, 7–24.

Du, H.-K., Xing Cao, J., Juan Xue, Y., & Jian Wang, X. (2015). Seismic facies analysis based on self-organizing map empirical mode decomposition. *Journal of Applied Geophysics*, *112*, 52–61.

Essenreiter, R., Karrenbach, M., & Treitel, S. (2001). Identification and classification of multiple reflections with self-organizing maps. *Geophysical Prospecting*, *49*, 341–352.

Higuti, R. T., Furukawa, C. M., & Adamowski, J. C. (2001). Characterization of lubricating oil using ultrasound. *Journal of the Brazilian Society of Mechanical Sciences*, *23*(4), 453–461. **(paper No 306)**.

Haskell, N. A. (1953). The dispersion of surface waves on multilayered media. *Bulletin of the Seismological Society of America*, *43*, 17–34.

Haskell, N. A. (1960). Crustal reflection of plane SH waves. *Journal of Geophysical Research*, *65*, 4147–4150.

Haskell, N. A. (1962). Crustal reflection of plane P and SV waves. *Journal of Geophysical Research*, *67*, 4751–4767.

Itzá, R., Iturrarán-Viveros, U., & Parra, J. O. (2016). Optimal implicit 2-D finite differences to model wave propagation in poroelastic media. *Geophysical Journal International*, *204*, 1–12.

Kennett, B., & Kerry, N. (1979). Seismic waves in a stratifed half-space. *Geophysical Journal of the Royal Astronomical Society*, *57*, 557–583.

Klose, C. (2006). Self-organizing maps for geoscientific data analysis: geological interpretation of multidimensional geophysical data. *Computer & Geosciences*, *10*, 265–277.

Kohonen, T. (1981). Automatic formation of topological maps of patterns in a self-organizing system. In: Oja, E., Simula, O. (eds.) Proc. 2nd Scand. Conf. on Image Analysis. Espoo: SuomenHahmontunnistustutkimuksen Seura, Finland, pp. 214–220.

Kohonen, T. (1982). Self-organized formation of topological correct feature maps. *Biological Cybernetics*, *43*, 59–69.

Kohonen, T. (2001). *Self-organizing maps* (3rd ed.). Berlin: Springer.

Kohonen, T. (2013). Essentials of the self-organizing map. *Neural Networks*, *37*, 52–65.

Konaté, A. A., Pan, H., Fang, S., Asim, S., Ziggah, Y. Y., Deng, C., et al. (2015). Capability of self-organizing map neural network in geophysical log data classification: case study from the CCSD-MH. *Journal of Applied Geophysics*, *118*, 37–46.

Liu, Y. (2014). Optimal staggered-grid finite-difference schemes based on least-squares for wave equation modelling. *Geophysical Journal International*, *197*, 1033–1047.

Liu, Y., & Sen, M. K. (2009). A practical implicit finite-difference method: examples from seismic modelling. *Journal of Geophysics and Engineering*, *6*, 231–249.

Masson, Y. J., Pride, S., & Nihei, K. (2006). Finite difference modeling of biots poroelastic equations at seismic frequencies. *Journal of Geophysical Research*, *11*, 1–13.

Özdenvar, T., & McMechan, G. (1997). Algorithms for staggered-grid computations for poroelastic, elastic, acoustic, and scalar wave equations. *Geophysical Prospecting*, *45*, 403–420.

Parra, J. O., Hackert, C. L., & Bennett, M. W. (2006). Permeability and porosity images based on *P*-wave surface seismic data: application to a south Florida aquifer. *Water Resources Research*, *42*, 1–14.

Parra, J. O., Iturrarán-Viveros, U., Parra, J. S., & Xu, P.-C. (2015). Attenuation and velocity estimation using rock physics and neural network methods for calibrating reflection seismograms. *Interpretation*, *3*(1), SA121–SA133.

Roy, A., Dowdell, B. L., & Marfut, K. J. (2013). Characterizing a Mississippian tripolitic chert reservoir using 3D unsupervised and supervised multiattibute seismic facies analysis: An example from Osage County, Oklahoma. *Interpretation*, *2013*, 109–124.

Roy, A., Marfut, K. J., 2012. Characterizing Mississippian tripolitic chert reservoir using unsupervised seismic facies analysis and well-logs: an example from Osage County, Oklahoma. In: SEG Expanded Abstracts. Tulsa Oklahoma, pp. 1-5.

Saraswat, P., & Sen, M. K. (2012). Artificial immune-based self-organizing maps for seismic-facies analysis. *Geophysics*, *77*(4), O45–O53.

Stankiewicz, J., Bauer, K., & Ryberg, T. (2010). Lithology classification from seismic tomography: additional constraints from surface waves. *Journal of African Earth Sciences*, *58*, 547–552.

Taner, M. T., Koheler, F., & Sheriff, R. E. (1979). Complex seismic trace analysis. *Geophysics*, *44*, 1041–1106.

Taner, M. T., Schuelke, J., ODoherty, R., Baysal, B., 1994. Seismic attributes: revisited. In: SEG Expanded Abstracts. Tulsa Oklahoma, pp. 1104-1106.

Tselentis, G.-A., Martakis, N., Paraskevopoulos, P., & Lois, A. (2011). High-resolution passive seismic tomography for 3D velocity, Poissons ratio v, and P-wave quality Q_P in the Delvina hydrocarbon field, southern Albania. *Geophysics*, *76*(2), B89–B112.

Vesanto, J., & Alhoniemi, E. (2000). Clustering of the Self-Organizing Map. *IEEE Transactions on Neural Networks*, *11*(3), 1483–1501.

Ward, J. H. J. (1963). Hierarchical Grouping to Optimize an Objective Function. *Journal of the American Statistical Association*, *58*, 236–244.

Zhu, X., & McMechan, G. A. (1991). Numerical simulation of seismic response of poroelastic reservoirs using Biot theory. *Geophysics*, *56*, 328–339.

(Received September 18, 2017, revised February 4, 2018, accepted February 13, 2018, Published online March 3, 2018)